Progress In Electromagnetics Research B, Vol. 88, 1–18, 2020

Moment Method Treatment of Corrugations with Fins over Ridges and Stratified Covers Using Dyadic Cavity and Multilayer Green's Functions for Studies of Higher-Order Diffraction Modes

Malcolm Ng Mou Kehn[1, 2, *]

Abstract—Herein presented is a numerical treatment of plane-wave scattering by gratings with metallic strip linings over both exterior surfaces of each conducting bar to create flanged groove apertures, which altogether is covered on both sides by multiple dielectric layers. The technique hinges on the method of moments that employs parallel-plate waveguide cavity dyadic Green's functions and a numerical spectral Green's function for planar stratified media along with Floquet concepts as well as the PEC equivalence theorem. In terms of reflection and transmission characteristics as well as surface wave modal dispersion, results computed by codes written based on this formulation are validated with those simulated by a commercial solver as well as in literature. Arising from the special complex geometry, the additional degrees of freedom offer measures for enhancing the performances of various applications such as beam deflectors, resolution of spectroscopic gratings, grating couplers, and grating pulse compression/decompression.

1. INTRODUCTION

Having proven vital to numerous engineering technologies in recent decades, metallic corrugations find applications as filters [1, 2], grating couplers [3–5], mode converters [6–9], modulators [10–12], beam deflectors [13–16], amongst many others. Through the years, numerous forms of methods to analyze or numerically treat such periodic structures have been reported [17–25]. However, none has yet to consider the special topology investigated in this paper, which is a periodic array of infinitely long penetrable conducting bars with wider strip covers or metal fins on both the lower and upper surfaces of each narrower ridge, which altogether is sheathed by multiple dielectric layers on both sides that sandwich the gratings. A rigorous full-wave modal analysis of plane-wave scattering by this structure is presented. Along with the PEC equivalence theorem, the approach entails the moment method using parallel-plate waveguide (PPW) cavity Green's functions and a numerical spectral-domain Green's function for planar stratified media accompanied by the Floquet theorem, the details of which are presented in Section 2. The former type of dyadic Green's functions is used to model the fields within the grooves of the corrugations, the information of which are bridged with those of the exterior multilayer structure derived from the latter form of Green's functions. Due to the full-wave nature of this computational technique, a multitude of Floquet modal harmonics is considered. Particular focus in this paper shall be on the higher-order diffraction modes.

A related but still dissimilar structure: the conductor grounded corrugated surface was studied in [26]. However, the analytical details remain substantially different and neither treatment is derivable from the other. Moreover, while reflection phase studies were conducted previously, investigations into

Received 1 May 2020, Accepted 27 June 2020, Scheduled 4 August 2020

* Corresponding author: Malcolm Ng Mou Kehn (malcolm.ng@ieee.org).

[1] Institute of Communications Engineering, College of Electrical and Computer Engineering, National Chiao Tung University, Taiwan.

[2] Center for mmWave Smart Radar Systems and Technologies, National Chiao Tung University, Taiwan.

the reflection and transmission properties of plane-wave incidences are instead relevant here. That prior work also considered only the zeroth-order Floquet harmonic whereas the dominant mode as well as higher diffraction orders is investigated here. Dielectric slab covers that were formerly neglected are also now considered. Furthermore, there were no studies earlier on how that related version could be put to practical use. Whereas in this paper, ways into which the new topology may enhance the performances of actual applications are presented, achieved through its many new degrees of parametric freedom that are absent from [26]. Finally, no experimental work was carried out in the latter whereas measurements performed on manufactured prototype gratings shall be reported in this paper.

Through the new structural as well as material attributes offered by the present special geometry, such as those afforded by dielectric slab covers loadable on both sides of the gratings, dielectric filling of the grooves, as well as flanged slits creatable by metallic fins loaded on the conducting bars, the performances of a multitude of applications can be boosted, such as grating couplers, spectroscopy, pulse compression and decompression gratings, grid polarizers, holography, and polarimetry, among many others in the fields of optics and antennas. This work is a thorough extension of the short paper [27], absent from which are the full mathematical details of the formulation as well as textual descriptions and pictorial illustrations of the concepts that shall be presented in this paper. In addition, ways in which the novel structure can enhance further applications absent earlier are also portrayed here.

In terms of reflection and transmission coefficients as well as modal surface-wave dispersion diagrams, computed results obtained from codes written based on the upcoming formulation shall be validated in Section 3 with those simulated by a commercial full-wave software solver and results from existing literature. Higher diffraction orders are then investigated in Section 4 and a convergence study is carried out in Section 5. Conclusions are then drawn in the final section.

2. THEORETICAL FORMULATION

The penetrable grating structure to be analyzed is shown in Fig. 1. The periodicity is along the x axis, with the period and groove width denoted as d_x and g, respectively. The depth (or height) of the gratings along z is given by h and the grooves are generally filled with a dielectric material of parameters $(\mu_{grv}, \varepsilon_{grv})$. Infinitesimally thin metallic wider strip plates are placed over the upper and lower faces of each narrower vertical conducting bar to form H-shaped dominos with iris-type slits across the groove apertures. The resultant widths of the upper and lower irises are defined as a_{up} and $a_{\ell o}$ respectively. When the widths of both strips equal that of the bar, thus shedding the iris-type slit apertures, the

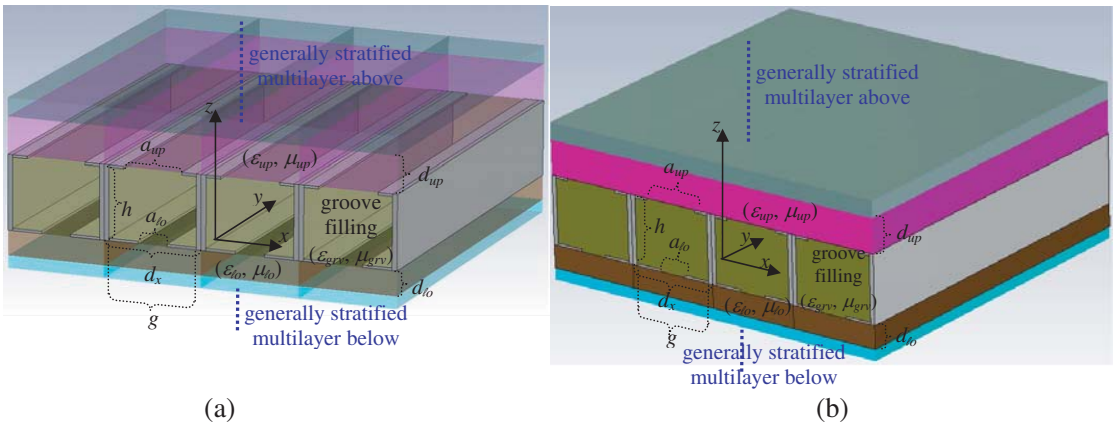

Figure 1. Corrugations with period d_x along x, depth h along z, generally dielectric filled grooves $(\varepsilon_{grv}, \mu_{grv})$, thin fin strip lined over both upper and lower ends of each ridge (bar) to create flanged groove apertures of widths a_{up} and $a_{\ell o}$, and generally sheathed by multiple layers of dielectric slabs on both sides that sandwich the gratings. (a) Translucent external dielectric slab covers to reveal the interior fin-loaded bars, and (b) fully opaque version.

structure then simplifies to conventional gratings. Multiple layers of planar dielectric sheaths cover each of the two sides of the gratings.

2.1. Orthonormalized Parallel-Plate Waveguide Modes

Consider first, the parallel-plate waveguide (PPW) in Fig. 2. For just the non-vanishing components, the orthonormalized PPW eigenmodal field functions for TM^z and TE^z modes are then written as follow (all other excluded components vanish).

$$\left[\begin{array}{cc} e^{\bar{\tau}}_{x_{p_{TM}}} & h^{\bar{\tau}}_{y_{p_{TM}}} \end{array}\right] = -\sqrt{\kappa_p/\bar{\varpi}}\left[\begin{array}{cc} \sqrt{Z^{\bar{\tau}}_{p_{TE}}} & \sqrt{Y^{\bar{\tau}}_{p_{TE}}} \end{array}\right] C^{\bar{\varpi}}_p \tag{1}$$

$$\left[\begin{array}{cc} e^{\bar{\tau}}_{y_{p_{TE}}} & h^{\bar{\tau}}_{x_{p_{TE}}} \end{array}\right] = \sqrt{2/\bar{\varpi}}\left[\begin{array}{cc} -\sqrt{Z^{\bar{\tau}}_{p_{TM}}} & \sqrt{Y^{\bar{\tau}}_{p_{TM}}} \end{array}\right] S^{\bar{\varpi}}_p \tag{2}$$

$$\left[\begin{array}{cc} e^{\bar{\tau}}_{z_{p_{TM}}} & h^{\bar{\tau}}_{z_{p_{TE}}} \end{array}\right] = \frac{\beta^{\bar{\varpi}}_{x_p}}{\gamma^{\bar{\tau}}_{z_p}\sqrt{\bar{\varpi}}}\left[\begin{array}{cc} \sqrt{\kappa_p Z^{\bar{\tau}}_{p_{TE}}}S^{\bar{\varpi}}_p & \sqrt{2Y^{\bar{\tau}}_{p_{TM}}}C^{\bar{\varpi}}_p \end{array}\right] \tag{3}$$

where

$$C^{\bar{\varpi}}_p = \cos X^{\bar{\varpi}}_p;\quad S^{\bar{\varpi}}_p = \sin X^{\bar{\varpi}}_p;\quad X^{\bar{\varpi}}_p = \beta^{\bar{\varpi}}_{x_p}x + (p\pi/2);\quad \beta^{\bar{\varpi}}_{x_p} = p\pi/\bar{\varpi}$$

$$Z^{\bar{\tau}}_{p_{TE}} = \gamma^{\bar{\tau}}_{z_p}\Big/(j\omega\varepsilon_{\bar{\tau}}) = \left(Y^{\bar{\tau}}_{p_{TE}}\right)^{-1};\quad Z^{\bar{\tau}}_{p_{TM}} = j\omega\mu_{\bar{\tau}}\Big/\gamma^{\bar{\tau}}_{z_p} = \left(Y^{\bar{\tau}}_{p_{TM}}\right)^{-1}$$

$$\kappa_p = \left\{\begin{array}{ll} 1, & \text{when } p=0 \\ 2, & \text{otherwise} \end{array}\right.,\quad \gamma^{\bar{\tau}}_{z_p} = \sqrt{\left(\beta^{\bar{\varpi}}_{x_p}\right)^2 - \omega^2\mu_{\bar{\tau}}\varepsilon_{\bar{\tau}}},$$

with $\bar{\varpi} = \left\{\begin{array}{cc} g & a_{\underline{\xi}} \end{array}\right\}$ and $\bar{\tau} = \left\{\begin{array}{cc} grv & ap,\underline{\xi} \end{array}\right\}$, $\underline{\xi} = \left\langle{}^{up}_{\ell o}\right\rangle$, whereby the left (first) and right (second) cases or items in such curly braces $\{\}$ throughout these equations correspond to one another. Note the further but independent triangular brace in the last expression, dissociated from the curly ones, the two elements of which dictate either the upper or lower aperture. The symbol g or a represents the width of either the groove or aperture (iris) region, respectively, as also labeled by the left case "*grv*" and right case "*ap*" in the curly braces.

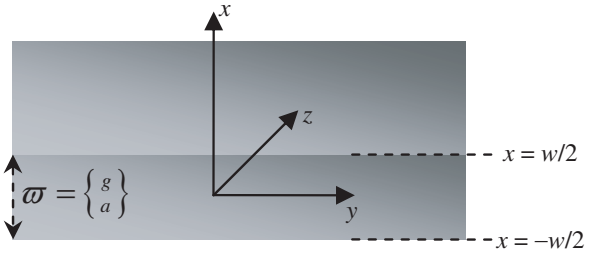

Figure 2. Parallel-plate waveguide with plate-separation ϖ that may represent g or a along x, for groove or aperture, respectively.

As an example of how the compact notations are unfolded, consider for instance, the left case item of Eq. (1), being $e^{\bar{\tau}}_{x_{p_{TM}}} = -\sqrt{\kappa_p/\bar{\varpi}}\sqrt{Z^{\bar{\tau}}_{p_{TE}}}C^{\bar{\varpi}}_p$. Then upon using the above symbolic representations, this latter expression is explicitly written as $e^{\{grv\quad ap,\langle{}^{up}_{\ell o}\rangle\}}_{x_{p_{TM}}} = -\sqrt{\frac{\kappa_p}{\{g\quad a_{\langle{}^{up}_{\ell o}\rangle}\}}\frac{\gamma^{\{grv\quad ap,\langle{}^{up}_{\ell o}\rangle\}}_{z_p}}{j\omega\varepsilon_{\{grv\quad ap,\langle{}^{up}_{\ell o}\rangle\}}}}\cos(\frac{p\pi x}{\{g\quad a_{\langle{}^{up}_{\ell o}\rangle}\}} + \frac{p\pi}{2})$. When this latter is further specialized to, say for example, the groove case, i.e., the left-side *grv* or g script case in curly braces, the expression becomes $e^{grv}_{x_{p_{TM}}} = -\sqrt{\frac{\kappa_p\gamma^{grv}_{z_p}}{j\omega\varepsilon_{grv}g}}\cos(\frac{p\pi x}{g} + \frac{p\pi}{2})$.

By these preceding equations, the PPW modes are orthonormalized, i.e.,

$$\int_{-\bar{w}/2}^{\bar{w}/2} \left[e^{\bar{\zeta}}_{x_{pr}}(x) h^{\bar{\zeta}}_{y_{u_w}}(x) - e^{\bar{\zeta}}_{y_{pr}}(x) h^{\bar{\zeta}}_{x_{u_w}}(x) \right] dx = \delta_{pr,uw}$$
$$\delta_{pr,uw} = \begin{cases} 1, & \text{only when } pr \equiv uw, \text{ i.e., } p = u,\ r \equiv w = TE \text{ or } TM \\ 0, & \text{otherwise} \end{cases} \tag{4}$$

as required for the derivation as well as utility of the PPW cavity Green's functions.

2.2. Expansion of PEC-Equivalent Magnetic Aperture Current into PPW Modal Basis Functions

The PEC equivalence theorem has been well explained in [28]. Also in this textbook, the use of this theorem to treat aperture problems is clearly described. As for the expansion of the unknown function (being the aperture magnetic current in the present context) into basis functions, this constitutes one of the pillars in the method of moments, which has been well documented in [29], another classical textbook. Upon invocation of PEC equivalence, the grooves of the gratings are filled up with PEC and the irises on both sides are replaced with equivalent magnetic strip current densities of infinite expanse along the y-direction; one being at $z = 0^+$ deemed as being the "upper one" while the other at $z = -h^-$, perceived as being the "lower one". These two magnetic slit current densities are succinctly expressed as:

$$\begin{aligned} \vec{M}^{\bar{\xi}}(x_s, z = \bar{\zeta}) &= e^{-jk_{y_0}y} \left[\hat{x} e^{ap}_x(x_s) + \hat{y} e^{ap}_y(x_s) \right] \times \{\pm\} \hat{z} \\ &= e^{-jk_{y_0}y} \left\{ \hat{x} \sum_{p_{TE}} A^{\bar{\xi}}_{p_{TE}} \tilde{m}^{\bar{\xi}}_{x_{p_{TE}}}(x_s, k_{y_0}) + \hat{y} \sum_{p_{TM}} A^{\bar{\xi}}_{p_{TM}} \tilde{m}^{\bar{\xi}}_{y_{p_{TM}}}(x_s, k_{y_0}) \right\} \end{aligned} \tag{5}$$

$$\tilde{m}^{\bar{\xi}}_{\underset{\sim}{\Omega}_{p_{\underset{\sim}{\chi}}}} = \{\pm\} \langle \pm \rangle e^{ap,\bar{\xi}}_{\underset{\sim}{\mho}_{p_{\underset{\sim}{\chi}}}} \tag{6}$$

$$\bar{\zeta} = \begin{Bmatrix} 0 \\ -h \end{Bmatrix}; \quad \bar{\xi} = \begin{Bmatrix} up \\ \ell o \end{Bmatrix}; \quad \underset{\sim}{\Omega} = \left\langle \begin{smallmatrix} x \\ y \end{smallmatrix} \right\rangle; \quad \underset{\sim}{\mho} = \left\langle \begin{smallmatrix} y \\ x \end{smallmatrix} \right\rangle; \quad \underset{\sim}{\chi} = \left\langle \begin{smallmatrix} TE \\ TM \end{smallmatrix} \right\rangle \tag{7}$$

whereby for each of the two kinds of braces, namely the curly and triangular brackets, the two items in either of them correspond to one another throughout the equation, but such tying up among any one brace type is independent of the other. The 's' subscript of x_s signifies that this is the source coordinate.

The term $e^{-jk_{y0}y}$ is pertinent to the treatment of plane wave scattering by the gratings, in connection with the illumination by an incident plane wave with a forcing wavenumber k_{y0} along y determining the dominant Floquet harmonic.

Again to showcase the way the concise expressions get unzipped, arbitrarily choosing the lower item within curly braces in Eq. (5) unfolds it to the following.

$$\begin{aligned} \vec{M}^{\ell o}(x_s, z = -h) &= e^{-jk_{y_0}y} \left\{ \hat{x} \sum_{p_{TE}} A^{\ell o}_{p_{TE}} \left[-e^{ap,\ell o}_{y_{p_{TE}}}(x_s, k_{y_0}) \right] + \hat{y} \sum_{p_{TM}} A^{\ell o}_{p_{TM}} \left(- \left[-e^{ap,\ell o}_{x_{p_{TM}}}(x_s, k_{y_0}) \right] \right) \right\} \\ &= e^{-jk_{y_0}y} \left\{ -\hat{x} \sum_{p_{TE}} A^{\ell o}_{p_{TE}} e^{ap,\ell o}_{y_{p_{TE}}}(x_s, k_{y_0}) + \hat{y} \sum_{p_{TM}} A^{\ell o}_{p_{TM}} e^{ap,\ell o}_{x_{p_{TM}}}(x_s, k_{y_0}) \right\} \end{aligned}$$

whereupon the use of Eqs. (1) and (2) in the paper further expands it to

$$\begin{aligned} \vec{M}^{\ell o}(x_s, z = -h) &= e^{-jk_{y_0}y} \left\{ \hat{x} \sum_{p_{TE}} A^{\ell o}_{p_{TE}} \sqrt{\frac{2j\omega\mu_{ap}}{a_{\ell o}\gamma^{ap}_{z_p}}} \sin\left(\frac{p_{TE}\pi x}{a_{\ell o}} + \frac{p_{TE}\pi}{2} \right) \right. \\ &\quad \left. + \hat{y} \sum_{p_{TM}} A^{\ell o}_{p_{TM}} \left[-\sqrt{\frac{\kappa_{p_{TM}}\gamma^{ap}_{z_p}}{j\omega\varepsilon_{ap}a_{\ell o}}} \cos\left(\frac{p_{TM}\pi x}{a_{\ell o}} + \frac{p_{TM}\pi}{2} \right) \right] \right\} \end{aligned}$$

which is the most explicit form.

2.3. *H*-Field Radiated into Grooves via PPW Cavity Green's Function

The groove region of the H-shaped bars, as shown in Fig. 3, is modeled as a two-ends shorted parallel-plate waveguide cavity, with propagation direction along z being perpendicular to the two infinitely-long (along y) metallic walls (parallel to xy plane, i.e., cross-sectional with respect to the propagation z-direction) serving as the shorting walls, at $z = -h$ and 0. On each of these two "end walls", upon PEC equivalence, locates an infinitely-long (along y) magnetic strip current aperture, which may generally be smaller than the cross-sectional shorting metallic strip-wall, so as to model an iris.

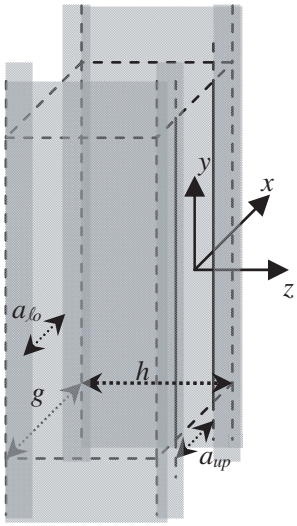

Figure 3. Groove region of corrugations modeled as a virtual parallel-plate waveguide (PPW) cavity, with "propagation" direction along z being perpendicular to the two infinitely-long (along y) metallic plate-walls (parallel to xy plane, i.e., cross-sectional with respect to the propagation z-direction) serving as the shorting walls, at $z = -h$ & 0. On either one of these two "end walls" locates an infinitely-long (along y) magnetic strip current aperture, which may generally be smaller than the cross-section of the PPW, so as to model an iris.

For the magnetic slit current source located at either of the two ends of the PPW groove namely at $z_s = 0$ or $-h$, and for H-field observation on either of these two bounding faces, i.e., $z_o = 0$ or $-h$, the observed transverse xy components of the H-field are collectively expressed by the following expression:

$$\vec{H}_t^{z_s=\zeta}(x_o, z_o = \underset{\sim}{\Theta}) = \langle \mp \rangle e^{-jk_{y0}y_o} \left[\sum_{p_{TM}=0}^{P'^{grv}_{TM}} \left\{ \begin{matrix} \Phi_{p_{TM}} \\ \Psi_{p_{TM}} \end{matrix} \right\} \vec{h}^{grv}_{t_{p_{TM}}}(x_o) \sum_{u_{TM}=0}^{U'^{ap}_{TM}} A^{\xi}_{u_{TM}} C^{\xi}_{x_u y_p} \right.$$
$$\left. - \sum_{p_{TE}=1}^{P^{grv}_{TE}} \left\{ \begin{matrix} \Phi_{p_{TE}} \\ \Psi_{p_{TE}} \end{matrix} \right\} \vec{h}^{grv}_{t_{p_{TE}}}(x_o) \sum_{u_{TE}=1}^{U^{ap}_{TE}} A^{\xi}_{u_{TE}} C^{\xi}_{y_u x_p} \right] \tag{8}$$

where $\bar{\zeta}' = \left\{ \begin{matrix} -h \\ 0 \end{matrix} \right\}$, $\underset{\sim}{\zeta} = \left\langle \begin{matrix} 0 \\ -h \end{matrix} \right\rangle$, $\underset{\sim}{\xi} = \left\langle \begin{matrix} up \\ \ell o \end{matrix} \right\rangle$, $\underset{\sim}{\Theta} = \left\langle \begin{matrix} \bar{\zeta} \\ \bar{\zeta}' \end{matrix} \right\rangle$, and also

$$\Phi_{p_\chi} = \coth\left(\gamma^{grv}_{z_{p_\chi}} h\right); \quad \Psi_{p_\chi} = \operatorname{csch}\left(\gamma^{grv}_{z_{p_\chi}} h\right);$$

$$C^{\bar{\xi}}_{x_u y_p} = \int_{-a_{\bar{\xi}}/2}^{a_{\bar{\xi}}/2} e^{ap,\bar{\xi}}_{x_{u_{TM}}}(x_s) h^{grv}_{y_{pTM}}(x_s) dx_s; \quad C^{\bar{\xi}}_{y_u x_p} = \int_{-a_{\bar{\xi}}/2}^{a_{\bar{\xi}}/2} e^{ap,\bar{\xi}}_{y_{u_{TE}}}(x_s) h^{grv}_{x_{pTE}}(x_s) dx_s$$

where $\vec{h}^{grv}_{t_{p_\chi}} = \hat{x} h^{grv}_{x_{p_\chi}} + \hat{y} h^{grv}_{y_{p_\chi}}$, with $\chi \equiv TM \text{or} TE$. Notice at this point the use of straight over-bar and curly underscore to signify curly and triangular braces, respectively, the item-to-item correspondence

in one brace type throughout the expression being independent of the other kind, as stressed earlier. The o and s subscripts of x denote the observation and source coordinates. The truncated numbers of TM and TE type PPW-cavity modes considered for the aperture fields are $U'^{ap}_{TM} = U^{ap}_{TM} - 1$ and U^{ap}_{TE} while $P'^{grv}_{TM} = P^{grv}_{TM} - 1$ and P'^{grv}_{TM} are those of the groove.

2.4. Fourier Transform of PEC-Equivalent Magnetic Strip-current over Iris-Type Aperture

The magnetic current of Eq. (5) may be restated as

$$\tilde{M}^{\bar{\xi}}_{\underset{\sim}{\Omega}}(x_s, z_s = \bar{\zeta}) = \sum_{u_{\bar{\chi}}=\underset{\sim}{\delta}}^{U^{ap}_{\underset{\sim}{\chi}}-\underset{\sim}{\delta}'} A^{\bar{\xi}}_{u_{\underset{\sim}{\chi}}} \tilde{m}^{\bar{\xi}}_{\underset{\sim}{\Omega}\,u_{\underset{\sim}{\chi}}}(x_s, k_{y_{n=0}}) \tag{9}$$

where $\underset{\sim}{\delta} = \left\langle {1 \atop 0} \right\rangle$; $\underset{\sim}{\delta}' = \left\langle {0 \atop 1} \right\rangle$. The single tilde signifies that these are already in the k_y spectral domain, evaluated at a single $k_{yn=0} = k \sin\theta_0 \sin\phi_0$, in which θ_0 and ϕ_0 are the incident angles of the incident plane wave (determining the dominant Floquet harmonic) that illuminates the corrugations from above, and k is the wavenumber of the medium exterior of the corrugations from which the excitation plane wave arrives (emerges).

Transforming these into spectral (k_{xm}, $k_{yn=0} = k_y^{ex}$) domain [involving just a single (line/contour) integration with respect to x_s], we write:

$$\tilde{\tilde{M}}^{\bar{\xi}}_{\underset{\sim}{\Omega}}(k_{x_m}, k_{y_{n=0}}, z_s = \bar{\zeta}) = \sum_{u_{\bar{\chi}}=\underset{\sim}{\delta}}^{U^{ap}_{\underset{\sim}{\chi}}-\underset{\sim}{\delta}'} A^{\bar{\xi}}_{u_{\underset{\sim}{\chi}}} \tilde{\tilde{m}}^{\bar{\xi}}_{\underset{\sim}{\Omega}\,u_{\underset{\sim}{\chi}}}(k_{x_m}, k_{y_{n=0}}) \tag{10}$$

$$\tilde{\tilde{m}}^{\bar{\xi}}_{\underset{\sim}{\Omega}\,u_{\underset{\sim}{\chi}}}(k_{x_m}, k_{y_{n=0}}) = \int_{-a_{\bar{\xi}}/2}^{a_{\bar{\xi}}/2} \tilde{m}^{\bar{\xi}}_{\underset{\sim}{\Omega}\,u_{\underset{\sim}{\chi}}}(x_s, k_{y_{n=0}}) e^{jk_{x_m}x_s} dx_s \tag{11}$$

with

$$k_{xm} = k_0 \sin\theta_0 \cos\phi_0 + 2m\pi/d_x, \tag{12}$$

such that the inverse transform from spectral k_x to spatial x domain only requires a summation over discrete spectral components defined by Eq. (12) due to the periodicity along only x (but not y) with period d_x. m is an integer; θ_0 and ϕ_0 are the angular coordinates determining the direction of the dominant Floquet modal beam, defined simply by the incidence angles of the incident plane wave (the primary excitation of the corrugations), and k_0 is the usual freespace wavenumber.

2.5. Spectral Magnetic Fields Radiated by Spectral Basis Magnetic Currents on Infinite PEC Surface

The spectral basis currents of Eq. (11) are subsequently employed as the secondary sources for the scattering scenario (as opposed to the primary incident plane wave source for the excitation scenario), which is the excitation of the smooth *uncorrugated* perfect electric conducting (PEC) planar structure, for which the grooves of the corrugations have been filled up with PEC (upon PEC equivalence). The spectral fields radiated by these spectral basis currents (placed just on the PEC surface) into the medium exterior to the corrugations are obtained from a numerical spectral Green's function for treating multilayer structures [30], the generic form of which is stated as

$$\tilde{\tilde{H}}^{(i)\tilde{\tilde{m}}^{\bar{\xi}}_{\underset{\sim}{\Omega}}\,u_{\underset{\sim}{\chi}}}_{w(z_o)} = \tilde{\tilde{G}}^{(i)M_{\underset{\sim}{\Omega}}}_{H_w(z_o)} \cdot \tilde{\tilde{m}}^{\bar{\xi}}_{\underset{\sim}{\Omega}\,u_{\underset{\sim}{\chi}}}, \tag{13}$$

where the w subscript may denote either x or y component of the radiated spectral H-field, and the superscript (i) represents the ith layer of the associated multilayer structure. The spectral dyadic Green's function G, appended by its dyadic dot operator, is characterized by superscript $M_{\underset{\sim}{\Omega}}$ signifying the magnetic current source type and its x or y component (via $\underset{\sim}{\Omega} = \langle {}^{x}_{y} \rangle$) of the secondary excitation source, whereas its subscript H_w indicates the type of the radiated field and its component. The driving spectral basis current is indicated as $\tilde{\tilde{m}}^{\bar{\xi}}_{\underset{\sim}{\Omega}\,u_{\chi}}$, which is from Eq. (11), and it is reminded that it pertains to a certain mth Floquet harmonic being the k_{xm} spectral component of Eq. (12) and in the present context, accompanied by a fixed dominant Floquet modal wavenumber component $k_{yn=0} = k \sin\theta_0 \sin\phi_0$. Note in Eq. (13) the explicit subscripted (z_o) which signifies the functionality in just the observation z_o coordinate level, which shall find convenience of use later. The complete details of this numerical spectral Green's function and its explicit expressions are found in the Appendix of [30].

2.6. Spatial Fields Radiated by Array of Magnetic Strip Currents into Region Exterior to Corrugations

As explained earlier at Eq. (12), the inverse transform of the spectral field of Eq. (13) is written as

$$\tilde{H}_{w(z_o)}^{\;(i)\tilde{m}^{\bar{\xi}}_{\underset{\sim}{\Omega}}\;u_{\chi}} = \frac{1}{d_x}\sum_{m} \tilde{\tilde{H}}_{w(z_o)}^{\;(i)\tilde{\tilde{m}}^{\bar{\xi}}_{\underset{\sim}{\Omega}}\;u_{\chi}} e^{-jk_{xm}x}; \quad H_{w(z_o)}^{\;(i)\tilde{m}^{\bar{\xi}}_{\underset{\sim}{\Omega}}\;u_{\chi}} = \tilde{H}_{w(z_o)}^{\;(i)\tilde{m}^{\bar{\xi}}_{\underset{\sim}{\Omega}}\;u_{\chi}} e^{-jk_{y0}y} \tag{14}$$

whereby the first equation in the above Eq. (14) amounts to the inverse transform from spectral k_x to spatial x domain, the resultant quantity on its left-hand side becoming a function of x but remaining in the spectral k_y domain with the absence of functionality in y (independent of it) and thus explaining its single tilde. The second equation constitutes the further inverse transformation of this latter (x, k_y) domain quantity to finally become a fully spatial-domain field that is a function of both x and y, totally free of tildes. This final quantity of Eq. (14) then constitutes the w-component of the spatial-domain H-field radiated by the x or y-directed *semi*-spatial (in x only) domain (u_{χ})th basis current $\tilde{m}^{\bar{\xi}}_{\underset{\sim}{\Omega}\,p_{\chi}}$ of Eq. (6). Assuming an odd M as the total truncated number of Floquet harmonics considered, the summation typically runs from $m = -(M-1)/2$ to $(M-1)/2$.

Subsequently, the total fields radiated by all basis currents would just entail a summation over the basis indices, each term scaled by an amplitude coefficient, according to Eq. (5) or its scalar form of Eq. (9), i.e.,

$$H_{w(z_o)}^{\;(i)\tilde{M}^{\bar{\xi}}_{\underset{\sim}{\Omega}}} = \sum_{u_{\bar{\chi}}=\delta}^{U^{ap}_{\chi}-\delta'} A^{\bar{\xi}}_{u_{\chi}} H_{w(z_o)}^{\;(i)\tilde{m}^{\bar{\xi}}_{\underset{\sim}{\Omega}}\;u_{\chi}} \tag{15}$$

whereby the superscript on the left-hand side, less the (i), is that of Eq. (9), which states the superposed combined sum contributions to the total magnetic current by numerous basis currents, each scaled by a certain amplitude coefficient, being thus far unknown and to be solved for. This represents the w-component of the spatial-domain H-field radiated by the x or y-directed magnetic current scatterer source components. It is noted that this remains only the scattered magnetic fields.

2.7. Two Multilayer Scenarios Bounded by PEC Half-Spaces

There are two different multilayer scenarios pertaining to either $\xi \equiv up$ or $\xi \equiv \ell o$; the upper or lower aperture surface of the grating. These two stratified configurations are illustrated in Fig. 4; Fig. 4(a) is for $\xi \equiv up$ while Fig. 4(b) is for $\xi \equiv \ell o$. The former, being PEC grounded at the bottom, is for the treatment of the upper half-space above the gratings that is generally stratified into multiple layers. Conversely, the latter depicts a multilayer scenario that is bounded at the top by PEC and is for treating the lower half-space below the gratings that is also generally stratified into layers. For Fig. 4(a), the

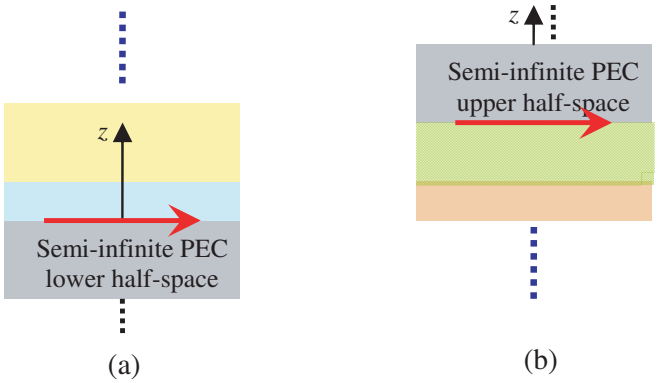

Figure 4. Multilayer scenarios associated with either (a) $\xi \equiv up$ that is PEC grounded at the bottom for treatment of upper half-space above gratings, or (b) $\xi \equiv \ell o$ that is PEC bounded at the top for treating lower half-space below gratings. In (a), a semi-infinite PEC takes up the lower half-space, above which is an upper half-space that is generally stratified into multiple dielectric layers. The lowermost one of these latter that interfaces with the grating is indexed as "i_{up}". In (b), a semi-infinite PEC takes up the upper half-space, below which is a lower half-space that is generally stratified into multiple dielectric layers. The uppermost one of these latter that interfaces with the grating is indexed as "$i_{\ell o}$". The arrows in both (a) and (b) depict the PEC-equivalence magnetic slit current densities.

lowermost layer of its upper stratified half-space which interfaces with the upper surface of the grating (transformed into a planar PEC ground) is indexed as "i_{up}", whereas in Fig. 4(b), the topmost layer of the lower stratified half-space that interfaces with the lower surface of the grating (transformed into a PEC ceiling) is labeled as "$i_{\ell o}$". Hence whenever the former index is involved, it is understood that the associated field is that of the multilayer scenario of Fig. 4(a) whereas when it is the latter that comes into play, Fig. 4(b) is the one that applies.

2.8. Boundary Conditions: Continuity of Tangential H-Fields across PPW Cavity Aperture

The boundary condition enforcing the continuities of the tangential magnetic field components across both the upper and lower iris-type apertures of just one unit cell of the gratings is stated as:

$$\left[\vec{H}_t^{z_s=0}(z_o=\bar{\zeta}) + \vec{H}_t^{z_s=-h}(z_o=\bar{\zeta})\right]_{-a_{\bar{\xi}}/2\le x_o\le a_{\bar{\xi}}/2} = \left\{ \begin{bmatrix} \hat{x}\left(H^{(i_{\bar{\xi}})\tilde{M}_x^{\bar{\xi}}}_{x(z_o=\bar{\zeta})} + H^{(i_{\bar{\xi}})\tilde{M}_y^{\bar{\xi}}}_{x(z_o=\bar{\zeta})}\right) \\ \hat{y}\left(H^{(i_{\bar{\xi}})\tilde{M}_x^{\bar{\xi}}}_{y(z_o=\bar{\zeta})} + H^{(i_{\bar{\xi}})\tilde{M}_y^{\bar{\xi}}}_{y(z_o=\bar{\zeta})}\right) \end{bmatrix} + \delta_{\bar{\xi}}^{1^\circ ex} \begin{bmatrix} \hat{x}H^{(i_{\bar{\xi}})1^\circ ex}_{x(z_o=\bar{\zeta})} \\ \hat{y}H^{(i_{\bar{\xi}})1^\circ ex}_{y(z_o=\bar{\zeta})} \end{bmatrix} \right\}_{-a_{\bar{\xi}}/2\le x_o\le a_{\bar{\xi}}/2} \tag{16}$$

$$\delta_{\bar{\xi}}^{1^\circ ex} = \begin{cases} 1 & \text{if prim excit plane-wave incid from} \\ & \{\substack{\text{above}\\\text{below}}\} \text{ gratings} \\ 0 & \text{otherwise} \end{cases}$$

noting the subscripted $-a_{\bar{\xi}}/2 \le x_o \le a_{\bar{\xi}}/2$ on both sides of Eq. (16), which expressly indicates that the tangential H-field continuities are enforced only across the upper and lower slits (of just one unit cell), excluding the PEC flanges or fins. This Eq. (16) unfolds into two separate equations, one for each of the upper and lower cases of the implicitly-entailed curly braces, which represent the boundary conditions for the upper and lower slit surfaces. The item in the second vector on the right-hand side, $H^{(i_{\bar{\xi}})1^\circ ex}_{w(z_o)}$, also acquired by the core routine that solves planar stratified structures in the spectral domain, represents

the known fields due to the primary excitation source (pertaining to the dominant Floquet harmonic associated with the forcing wavenumber determined by the angular coordinates θ_0 and ϕ_0 of the incident plane wave direction) which radiates in the multilayer structure that is bounded by a semi-infinite half space of bare (or smooth) *uncorrugated* PEC. As before, the superscript $(i_{\bar{\xi}})$ denotes which multilayer scenario of Fig. 4 applies. The explicit representations of this $H_w^{1^\circ ex}$ are also obtainable from [30].

2.9. Galerkin Weighting and Construction of Matrices

The technique of using the basis function as the weighting function is called the Galerkin's method [31]. With $\bar{e}_{t_{v_\psi}}^{ap,\bar{\xi}} = \hat{x}e_{x_{v_\psi}}^{ap,\bar{\xi}} + \hat{y}e_{y_{v_\psi}}^{ap,\bar{\xi}}$, where ψ may denote TE or TM, then taking $\int_{-a_{\bar{\xi}}/2}^{a_{\bar{\xi}}/2} [\bar{e}_{t_{v_\psi}}^{ap,\bar{\xi}}(x_o) \times \_\_ \cdot \hat{z}]dx_o$ throughout the boundary condition (16), for $v_{TE} = 1, 2, \ldots, U_{TE}^{ap}$ and $v_{TM} = 0, 1, \ldots, U_{TM}^{ap} - 1$, for each of the two cases in the curly braces of $\underline{\xi}$, a total number of equations $[2(U_{TE}^{ap} + U_{TM}^{ap})]$ that equals the number of unknown coefficients of the basis functions expanding the aperture magnetic currents are generated. This system of equation can be cast into a matrix equation. The intermediate matrices that build up to this matrix equation are as follows.

Before proceeding, some definitions have to be first laid out. In all upcoming relations, the following generic form applies:

$$[\underline{M}(\alpha_i, \beta_j)]_{P\times Q} \mapsto Z_{ij} \tag{17}$$

The left-hand side square-bracketed quantity named as M is a matrix with a size of P rows by Q columns as specified by the exterior subscript. The $(\alpha_i,\ \beta_j)$ expresses the two sequentially-running entities α and β indexed respectively by positive integers i and j that constitute the row and column dimensions, respectively. In other words, the element occupying the ith row and jth column is given by the right-hand side quantity Z_{ij} which is characterized by the ith and jth integer indices of these α and β. Subsequently, the symbol $\mapsto$ denotes "whose (i, j)th element is". By the rate of Eq. (17), $[M(\alpha_i, \alpha_j)]_{P\times P}$ represents a square diagonal matrix whose (i, i)th element is given by Z_{ii}, thus entailing just one characterizing variable α.

In a similar but modified fashion of Eq. (17), column and row vectors are also generically written as:

$$[\underline{V}(\alpha_i, 1)]_{P\times 1} \mapsto Z_i; \quad [\underline{V}(1, \alpha_i)]_{1\times P} \mapsto Z_i \tag{18}$$

With these definitions established, the various matrices are ready to be written.

The first one is stated as:

$$\left[\underline{\underset{\sim}{A}}_w^{\chi,\bar{\xi}}(m, u_\chi)\right]_{M\times U_\chi^{ap}} \mapsto (1/d_x)\, \tilde{\tilde{H}}_{w(z_o=\bar{\zeta})}^{(i_{\bar{\xi}})\tilde{\tilde{m}}_\Omega^{\bar{\xi}}{}_{u_\chi}} \tag{19}$$

for $w = x$ or y. Due to the three characterizing items: w, $\underset{\sim}{\chi}$, and $\bar{\xi}$, each with two options, just this Eq. (10) alone unfolds to $2^3 = 8$ distinct matrices.

Subsequent ones are written as:

$$\left[\underline{B}_\mho^{\chi,\bar{\xi}}(v_\chi, m)\right]_{U_\chi^{ap}\times M} \mapsto \int_{-a_{\bar{\xi}}/2}^{a_{\bar{\xi}}/2} e_{\mho}^{ap,\bar{\xi}}{}_{v_\chi}(x_o) e^{-jk_{x_m}x_o} dx_o \tag{20}$$

$$\left[C_\chi^{\bar{\xi}}(u_\chi, p_\chi)\right]_{U_\chi^{ap}\times P_\chi^{grv}} \mapsto \int_{-a_{\bar{\xi}}/2}^{a_{\bar{\xi}}/2} e_{\mho}^{ap,\bar{\xi}}{}_{u_\chi}(x_s) h_{\Omega}^{grv}{}_{p_\chi}(x_s) dx_s \tag{21}$$

Next, the following diagonal matrices are defined:

$$\left[\underline{\Phi}_{p_{\mathfrak{X}}}(p_{\mathfrak{X}},p_{\mathfrak{X}})\right]_{P_{\mathfrak{X}}^{grv}\times P_{\mathfrak{X}}^{grv}}\mapsto\coth(\gamma_{z_{p_{\mathfrak{X}}}}^{grv}h) \tag{22}$$

$$\left[\underline{\Psi}_{p_{\mathfrak{X}}}(p_{\mathfrak{X}},p_{\mathfrak{X}})\right]_{P_{\mathfrak{X}}^{grv}\times P_{\mathfrak{X}}^{grv}}\mapsto\operatorname{csch}(\gamma_{z_{p_{\mathfrak{X}}}}^{grv}h) \tag{23}$$

whose diagonal $(i,\ i)$th elements are respectively $\coth(\gamma_{z_{p_{\mathfrak{X}}}}^{grv}{}_{i}h)$ and $\operatorname{csch}(\gamma_{z_{p_{\mathfrak{X}}}}^{grv}{}_{i}h)$ whereby $p_{\chi i}$ is the ith integer index of the sequential variable $p_{\underset{\sim}{\chi}}$, for both modal cases of $\underset{\sim}{\chi}=\left\langle{}_{TM}^{TE}\right\rangle^{i}$.

The following column vectors are also constructed.

$$\left[\underline{V}_{\underset{\sim}{\chi}}^{\bar{\xi}}(v_{\underset{\sim}{\chi}},1)\right]_{U_{\mathfrak{X}}^{ap}\times 1}\mapsto\langle\pm\rangle\,\delta_{\bar{\xi}}^{1^{\circ}ex}H_{\Omega}^{1^{\circ}ex}\int_{-a_{\bar{\xi}}/2}^{a_{\bar{\xi}}/2}e_{\mathfrak{V}}^{ap,\bar{\xi}}{}_{v_{\mathfrak{X}}}(x_o)e^{-jk_{x_{m=0}}x_o}dx_o \tag{24}$$

$$\left[\underline{V}_{final}(v,1)\right]_{2(U_{TM}^{ap}+U_{TE}^{ap})\times 1}=\left\{\begin{array}{l}\left[V_{TM}^{up}(v_{TM},1)\right]_{U_{TM}^{ap}\times 1}\\ \left[V_{TE}^{up}(v_{TE},1)\right]_{U_{TE}^{ap}\times 1}\\ \left[V_{TM}^{\ell o}(v_{TM},1)\right]_{U_{TM}^{ap}\times 1}\\ \left[V_{TE}^{\ell o}(v_{TE},1)\right]_{U_{TE}^{ap}\times 1}\end{array}\right\} \tag{25}$$

this latter being the finalized column vector containing the known excitation terms that shall be placed on the right-hand side of the upcoming ultimate matrix equation.

2.10. Matrix Operations and Construction of Ultimate Moment-Method Matrix Equation

With the foregoing intermediate matrices laid out, the following matrix operations are then performed.

$$\begin{aligned}\left[\underline{M}_{11}(v_{TM},u_{TM})\right]_{U_{TM}^{ap}\times U_{TM}^{ap}}&=\left[\underline{B}_{x}^{TM,up}(v_{TM},m)\right]_{U_{TM}^{ap}\times M}\left[\underline{A}_{y}^{TM,up}(m,u_{TM})\right]_{M\times U_{TM}^{ap}}\\&+\left\{\left[\underline{C}_{TM}^{up}(v_{TM},p_{TM})\right]_{U_{TM}^{ap}\times P_{TM}^{grv}}\left[\underline{\Phi}_{p_{TM}}(p_{TM},p_{TM})\right]_{P_{TM}^{grv}\times P_{TM}^{grv}}\right\}_{U_{TM}^{ap}\times \mathrm{P}_{TM}^{grv}}\\&\left[\left[\left\{\left[\underline{C}_{TM}^{up}(u_{TM},p_{TM})\right]_{U_{TM}^{ap}\times P_{TM}^{grv}}\right\}^{\mathrm{T}}\right]\right]_{P_{TM}^{grv}\times U_{TM}^{ap}}\end{aligned} \tag{26}$$

$$\left[\underline{M}_{12}(v_{TM},u_{TE})\right]_{U_{TM}^{ap}\times U_{TE}^{ap}}=\left[\underline{B}_{x}^{TM,up}(v_{TM},m)\right]_{U_{TM}^{ap}\times M}\left[\underline{A}_{y}^{TE,up}(m,u_{TE})\right]_{M\times U_{TE}^{ap}} \tag{27}$$

$$\begin{aligned}\left[\underline{M}_{13}(v_{TM},u_{TM})\right]_{U_{TM}^{ap}\times U_{TM}^{ap}}&=-\left\{\left[\underline{C}_{TM}^{up}(v_{TM},p_{TM})\right]_{U_{TM}^{ap}\times P_{TM}^{grv}}\left[\underline{\Psi}_{p_{\mathfrak{X}}}(p_{TM},p_{TM})\right]_{P_{TM}^{grv}\times P_{TM}^{grv}}\right\}_{U_{TM}^{ap}\times \mathrm{P}_{TM}^{grv}}\\&\left[\left[\left\{\left[\underline{C}_{TM}^{\ell o}(u_{TM},p_{TM})\right]_{U_{TM}^{ap}\times P_{TM}^{grv}}\right\}^{\mathrm{T}}\right]\right]_{P_{TM}^{grv}\times U_{TM}^{ap}}\end{aligned} \tag{28}$$

$$\left[\underline{M}_{14}(v_{TM},u_{TE})\right]_{U_{TM}^{ap}\times U_{TE}^{ap}}=\left[\underline{0}\right]_{U_{TM}^{ap}\times U_{TE}^{ap}} \tag{29}$$

$$\left[\underline{M}_{21}(v_{TE},u_{TM})\right]_{U_{TE}^{ap}\times U_{TM}^{ap}}=-\left[\underline{B}_{y}^{TE,up}(v_{TE},m)\right]_{U_{TE}^{ap}\times M}\left[\underline{A}_{x}^{TM,up}(m,u_{TM})\right]_{M\times U_{TM}^{ap}} \tag{30}$$

$$\begin{aligned}\left[\underline{M}_{22}(v_{TE},u_{TE})\right]_{U_{TE}^{ap}\times U_{TE}^{ap}}&=-\left[\underline{B}_{y}^{TE,up}(v_{TE},m)\right]_{U_{TE}^{ap}\times M}\left[\underline{A}_{x}^{TE,up}(m,u_{TE})\right]_{M\times U_{TE}^{ap}}\\&+\left\{\left[\underline{C}_{TE}^{up}(v_{TE},p_{TE})\right]_{U_{TE}^{ap}\times P_{TE}^{grv}}\left[\underline{\Phi}_{p_{TE}}(p_{TE},p_{TE})\right]_{P_{TE}^{grv}\times P_{TE}^{grv}}\right\}_{U_{TE}^{ap}\times \mathrm{P}_{TE}^{grv}}\\&\left[\left[\left\{\left[\underline{C}_{TE}^{up}(u_{TE},p_{TE})\right]_{U_{TE}^{ap}\times P_{TE}^{grv}}\right\}^{\mathrm{T}}\right]\right]_{P_{TE}^{grv}\times U_{TE}^{ap}}\end{aligned} \tag{31}$$

$$[\underline{M}_{23}(v_{TE},u_{TM})]_{U_{TE}^{ap}\times U_{TM}^{ap}} = [\underline{0}]_{U_{TE}^{ap}\times U_{TM}^{ap}} \tag{32}$$

$$[\underline{M}_{24}(v_{TE},u_{TE})]_{U_{TE}^{ap}\times U_{TE}^{ap}} = -\left\{[\underline{C}_{TE}^{up}(v_{TE},p_{TE})]_{U_{TE}^{ap}\times P_{TE}^{grv}}[\underline{\Psi}_{p_{TE}}(p_{TE},p_{TE})]_{P_{TE}^{grv}\times P_{TE}^{grv}}\right\}_{U_{TE}^{ap}\times \mathrm{P}_{TE}^{grv}} \left[\left[\left\{[\underline{C}_{TE}^{\ell o}(u_{TE},p_{TE})]_{U_{TE}^{ap}\times P_{TE}^{grv}}\right\}^{\mathrm{T}}\right]\right]_{P_{TE}^{grv}\times U_{TE}^{ap}} \tag{33}$$

$$[\underline{M}_{31}(v_{TM},u_{TM})]_{U_{TM}^{ap}\times U_{TM}^{ap}} = \left\{[\underline{C}_{TM}^{\ell o}(v_{TM},p_{TM})]_{U_{TM}^{ap}\times P_{TM}^{grv}}[\underline{\Psi}_{p_{TM}}(p_{TM},p_{TM})]_{P_{TM}^{grv}\times P_{TM}^{grv}}\right\}_{U_{TM}^{ap}\times \mathrm{P}_{TM}^{grv}} \left[\left[\left\{[\underline{C}_{TM}^{up}(u_{TM},p_{TM})]_{U_{TM}^{ap}\times P_{TM}^{grv}}\right\}^{\mathrm{T}}\right]\right]_{P_{TM}^{grv}\times U_{TM}^{ap}} \tag{34}$$

$$[\underline{M}_{32}(v_{TM},u_{TE})]_{U_{TM}^{ap}\times U_{TE}^{ap}} = [\underline{0}]_{U_{TM}^{ap}\times U_{TE}^{ap}} \tag{35}$$

$$[\underline{M}_{33}(v_{TM},u_{TM})]_{U_{TM}^{ap}\times U_{TM}^{ap}} = \left[\underline{B}_x^{TM,\ell o}(v_{TM},m)\right]_{U_{TM}^{ap}\times M}[\underline{A}_y^{TM,\ell o}(m,u_{TM})]_{M\times U_{TM}^{ap}} - \left\{[\underline{C}_{TM}^{\ell o}(v_{TM},p_{TM})]_{U_{TM}^{ap}\times P_{TM}^{grv}}[\underline{\Phi}_{p_{TM}}(p_{TM},p_{TM})]_{P_{TM}^{grv}\times P_{TM}^{grv}}\right\}_{U_{TM}^{ap}\times \mathrm{P}_{TM}^{grv}} \left[\left[\left\{\left[\underline{C}_{TM}^{\ell o}(u_{TM},p_{TM})\right]_{U_{TM}^{ap}\times P_{TM}^{grv}}\right\}^{\mathrm{T}}\right]\right]_{P_{TM}^{grv}\times U_{TM}^{ap}} \tag{36}$$

$$[\underline{M}_{34}(v_{TM},u_{TE})]_{U_{TM}^{ap}\times U_{TE}^{ap}} = \left[\underline{B}_x^{TM,\ell o}(v_{TM},m)\right]_{U_{TM}^{ap}\times M}[\underline{A}_y^{TE,\ell o}(m,u_{TE})]_{M\times U_{TE}^{ap}} \tag{37}$$

$$[\underline{M}_{41}(v_{TE},u_{TM})]_{U_{TE}^{ap}\times U_{TM}^{ap}} = [\underline{0}]_{U_{TE}^{ap}\times U_{TM}^{ap}} \tag{38}$$

$$[\underline{M}_{42}(v_{TE},u_{TE})]_{U_{TE}^{ap}\times U_{TE}^{ap}} = \left\{[\underline{C}_{TE}^{\ell o}(v_{TE},p_{TE})]_{U_{TE}^{ap}\times P_{TE}^{grv}}[\underline{\Psi}_{p_{TE}}(p_{TE},p_{TE})]_{P_{TE}^{grv}\times P_{TE}^{grv}}\right\}_{U_{TE}^{ap}\times \mathrm{P}_{TE}^{grv}} \left[\left[\left\{[\underline{C}_{TE}^{up}(u_{TE},p_{TE})]_{U_{TE}^{ap}\times P_{TE}^{grv}}\right\}^{\mathrm{T}}\right]\right]_{P_{TE}^{grv}\times U_{TE}^{ap}} \tag{39}$$

$$[\underline{M}_{43}(v_{TE},u_{TM})]_{U_{TE}^{ap}\times U_{TM}^{ap}} = -\left[\underline{B}_y^{TE,\ell o}(v_{TE},m)\right]_{U_{TE}^{ap}\times M}[\underline{A}_x^{TM,\ell o}(m,u_{TM})]_{M\times U_{TM}^{ap}} \tag{40}$$

$$[\underline{M}_{44}(v_{TE},u_{TE})]_{U_{TE}^{ap}\times U_{TE}^{ap}} = -\left[\underline{B}_y^{TE,\ell o}(v_{TE},m)\right]_{U_{TE}^{ap}\times M}[\underline{A}_x^{TE,\ell o}(m,u_{TE})]_{M\times U_{TE}^{ap}} - \left\{[\underline{C}_{TE}^{\ell o}(v_{TE},p_{TE})]_{U_{TE}^{ap}\times P_{TE}^{grv}}[\underline{\Phi}_{p_{TE}}(p_{TE},p_{TE})]_{P_{TE}^{grv}\times P_{TE}^{grv}}\right\}_{U_{TE}^{ap}\times \mathrm{P}_{TE}^{grv}} \left[\left[\left\{[\underline{C}_{TE}^{\ell o}(u_{TE},p_{TE})]_{U_{TE}^{ap}\times P_{TE}^{grv}}\right\}^{\mathrm{T}}\right]\right]_{P_{TE}^{grv}\times U_{TE}^{ap}} \tag{41}$$

These 16 submatrices are then cascaded to form the final matrix expressed as:

$$\left[\underline{M}_{final}\right]_{2\left(U_{TM}^{ap}+U_{TE}^{ap}\right)\times 2\left(U_{TM}^{ap}+U_{TE}^{ap}\right)} = \begin{Bmatrix} \underline{M}_{11} & \underline{M}_{12} & \underline{M}_{13} & \underline{M}_{14} \\ \underline{M}_{21} & \underline{M}_{22} & \underline{M}_{23} & \underline{M}_{24} \\ \underline{M}_{31} & \underline{M}_{32} & \underline{M}_{33} & \underline{M}_{34} \\ \underline{M}_{41} & \underline{M}_{42} & \underline{M}_{43} & \underline{M}_{44} \end{Bmatrix} \tag{42}$$

Finally, the ultimate matrix equation is stated as:

$$\left[\underline{M}_{final}\right]_{2\left(U_{TM}^{ap}+U_{TE}^{ap}\right)\times 2\left(U_{TM}^{ap}+U_{TE}^{ap}\right)}\left[\underline{A}_{final}\right]_{2\left(U_{TM}^{ap}+U_{TE}^{ap}\right)\times 1} = \left[\underline{V}_{final}(v,1)\right]_{2\left(U_{TM}^{ap}+U_{TE}^{ap}\right)\times 1} \tag{43}$$

where

$$\left[\underline{A}_{final}\right]_{2\left(U_{TM}^{ap}+U_{TE}^{ap}\right)\times 1} = \begin{bmatrix} \underline{A}_{u_{TM}}^{up} & \underline{A}_{u_{TE}}^{up} & \underline{A}_{u_{TM}}^{\ell o} & \underline{A}_{u_{TE}}^{\ell o} \end{bmatrix} \tag{44}$$

with the row vector:

$$\left[\underline{A}_{u_{\chi}}^{\bar{\xi}}(1,u_{\chi})\right]_{1\times U_{\chi}^{ap}} \mapsto A_{u_{\chi}}^{\bar{\xi}} \tag{45}$$

Eq. (43) can then be solved for the vector containing the unknown coefficients via matrix inversion, thereby concluding the solution treatment of the entire structure.

3. VALIDATION WITH COMMERCIAL SOFTWARE SOLVER

Two groups of numerical results computed by the entirely self-developed numerical code based on the present formulation are now presented: (A) spectra of reflection and transmission coefficients, and (B) modal surface-wave dispersion diagrams. These results shall be compared with those generated by a commercial full-wave simulator: CST Microwave Studio®; henceforth referred to simply as CST. It is stated at this point that for all upcoming computed results, the permeabilities of all regions throughout the whole structure are assumed to be that of free space, i.e., $\mu_{grv} = \mu_{\ell o} = \mu_{up} = \mu_0$. The dominant $m = 0$ Floquet mode is also assumed in this present section, until Section 4.

3.1. Reflection and Transmission Spectral Diagrams

Presented in Fig. 5 is the validation of an arbitrary case in terms of reflection and transmission coefficients plotted against frequency, for normal incidence ($\theta_{inc} = \theta_0 = 0$ with $\phi_{inc} = 9°$) of a TE^z y-polarized plane wave onto a grating with $d_x = 4$ mm, $\varepsilon_{grv}/\varepsilon = 4$, $h = 3$ mm, $g = 3.6$ mm, $a_{up} = a_{\ell o} = 3.2$ mm, $\varepsilon_{\ell o}/\varepsilon = 2$, $d_{\ell o} = 1$ mm, $\varepsilon_{up}/\varepsilon = 3$, $d_{up} = 2$ mm. The agreements between the curves computed by the present modal method and those simulated by CST are seen to be excellent for both the reflection and transmission.

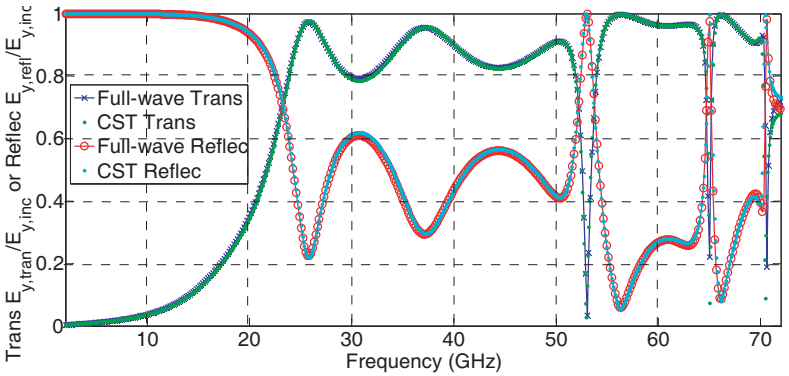

Figure 5. Validation with CST of variations of $m = 0$ modal transmission and reflection coefficients with frequency for TM^z polarized plane-wave incidence with $\theta_{inc} = 0$, $\phi_{inc} = 90°$ (thus y-polarization), for $d_x = 4$ mm, $\varepsilon_{grv}/\varepsilon_0 = 4$, $h = 3$ mm, $g = 3.6$ mm, $a_{up} = a_{\ell o} = 3.2$ mm, $\varepsilon_{\ell o}/\varepsilon_0 = 2$, $d_{\ell o} = 1$ mm, $\varepsilon_{up}/\varepsilon_0 = 3$, $d_{up} = 2$ mm.

The same can be said of the upcoming transmission and reflection spectra of Fig. 6 for the same topology of gratings, but now for $\theta_{inc} = 30°$ and $\phi_{inc} = 0$. Evidently, the traces of the present method and CST are again almost indistinguishable.

3.2. Surface-Wave Dispersion Diagram

Validation of the formulated modal approach is also carried out in terms of the surface-wave modal dispersion diagram. For another arbitrary case of $d_x = 2$ mm, $\varepsilon_{grv}/\varepsilon = 3$, $h = 1$ mm, $g = a_{up} = a_{\ell o} = 1.8$ mm (no fins), and $\varepsilon_{\ell o}/\varepsilon = \varepsilon_{up}/\varepsilon = 1.0$ (uncovered on both sides), Fig. 7 conveys the dispersion diagram for surface-wave propagation along x perpendicular to the gratings, i.e., $\phi = 0$, generated using the present method and CST. The agreement between both tools is seen to be good as well.

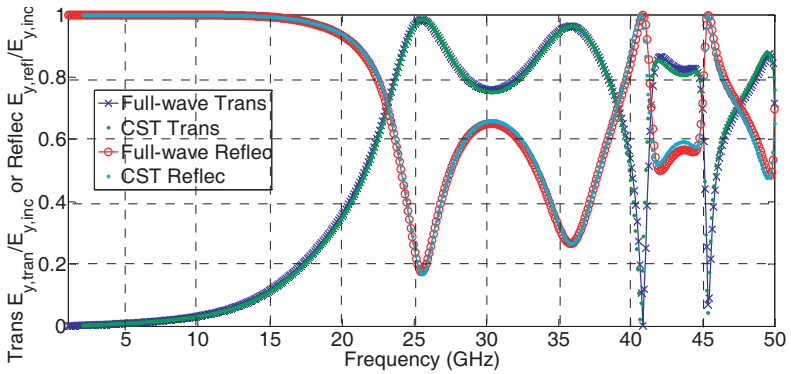

Figure 6. Validation with CST of variations of $m = 0$ modal transmission and reflection coefficients with frequency for TE^z polarized plane-wave incidence with $\theta_{inc} = 30°$, $\phi_{inc} = 0$ (thus y-polarization), for $d_x = 4\,\text{mm}$, $\varepsilon_{grv}/\varepsilon_0 = 4$, $h = 3\,\text{mm}$, $g = 3.6\,\text{mm}$, $a_{up} = a_{\ell o} = 3.2\,\text{mm}$, $\varepsilon_{\ell o}/\varepsilon_0 = 2$, $d_{\ell o} = 1\,\text{mm}$, $\varepsilon_{up}/\varepsilon_0 = 3$, $d_{up} = 2\,\text{mm}$.

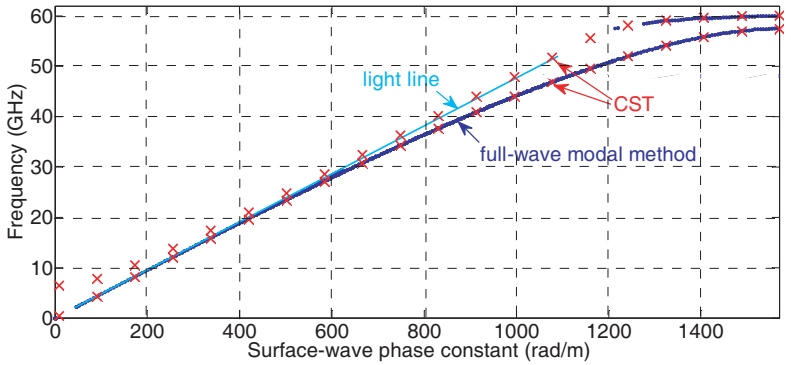

Figure 7. Validation with CST of surface-wave dispersion diagram with $\phi_0 = k_{y0} = 0$ (propagation along x), for $d_x = 2\,\text{mm}$, $\varepsilon_{grv}/\varepsilon_0 = 3$, $h = 1\,\text{mm}$, $g = a_{up} = a_{\ell o} = 1.8\,\text{mm}$, $\varepsilon_{\ell o}/\varepsilon_0 = \varepsilon_{up}/\varepsilon_0 = 1.0$ (uncovered on both sides).

4. HIGHER DIFFRACTION ORDERS OF FLOQUET HARMONICS

For any higher ordered Floquet harmonic modal index $m \neq 0$ along with a real incidence angle $\theta_{inc} = \theta_0$ (between 0 and π) and grating period d_x, the frequency f_m^{crit} beyond which this mth diffraction order grating lobe starts to appear in real space is given by

$$f_m^{crit} = \frac{m}{d_x\sqrt{\mu_0\varepsilon_0}\,[\text{sgn}(m) - \sin\theta_0]} \tag{46}$$

where sgn is the sign function. This so-called *critical* frequency constitutes the transition boundary between slow surface waves in the imaginary regime and fast space waves in the visible region. As the frequency rises further beyond f_m^{crit}, this mth Floquet harmonic (now a fast space wave) steers away from its grazing propagation direction and moves deeper into the visible fast-wave region with progressively reduced component of its wave-vector along the surface. A formula to prescribe this direction, denoted as θ_m^{diff} (real angle measured from the vertical axis perpendicular to the gratings) is governed by:

$$\theta_m^{diff} = \sin^{-1}\left[\sin\theta_0 + (m\lambda_0/d_x)\right] \tag{47}$$

where $\lambda_0 = 1/[\,f\sqrt{(\mu_0\varepsilon_0)}]$ is the free space wavenumber. This relation thus connects θ_m^{diff}, θ_0, f $(= c/\lambda_0)$ and d_x together.

As a corroboration with an existing result in [32], Fig. 8 presents the transmission spectrum of the $m = -1$ diffraction order for TM^z polarized plane-wave incidence with $\theta_{inc} = 31.5°$, $\phi_{inc} = 0$ onto a

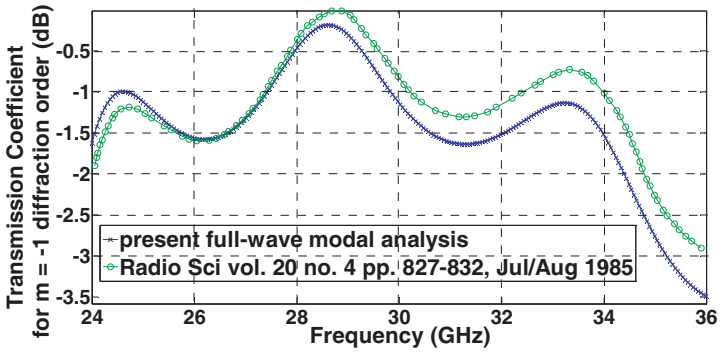

Figure 8. Validation with Ref. [32] of variation with frequency of transmission coefficient of $m = -1$ Floquet harmonic for TM^z polarized plane-wave incidence with $\theta_{inc} = 31.5°$, $\phi_{inc} = 0$, for $d_x = 10\,\text{mm}$, $\varepsilon_{grv}/\varepsilon_0 = 1$, $h = 20.6\,\text{mm}$, $g = 7.6\,\text{mm}$, $a_{up} = a_{\ell o} = g$, $\varepsilon_{\ell o}/\varepsilon_0 = \varepsilon_{up}/\varepsilon_0 = 1$.

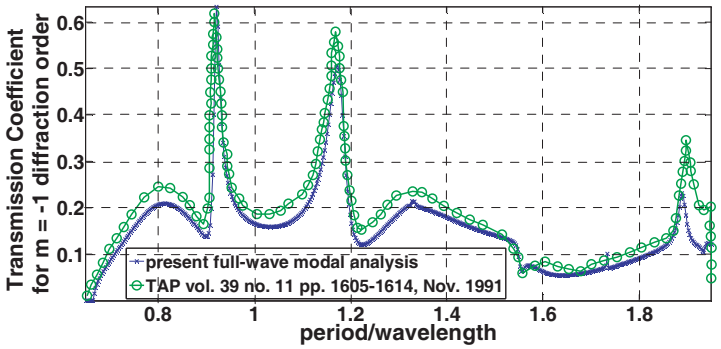

Figure 9. Validation with Ref. [33] of variation with period relative to wavelength of transmission coefficient of $m = -1$ Floquet harmonic with $\theta_{inc} = 30°$, $\phi_{inc} = 0$, for $d_x = 4\,\text{mm}$, $\varepsilon_{grv}/\varepsilon_0 = 4$, $h = 1.6\,\text{mm}$, $g = 2.4\,\text{mm}$, $a_{up} = a_{\ell o} = g$, $\varepsilon_{\ell o}/\varepsilon_0 = \varepsilon_{up}/\varepsilon_0 = 1$.

grating with $d_x = 10\,\text{mm}$, $\varepsilon_{grv}/\varepsilon_0 = 1$, $h = 20.6\,\text{mm}$, $g = 7.6\,\text{mm}$, $a_{up} = a_{\ell o} = g$ (no fins), and $\varepsilon_{\ell o}/\varepsilon_0 = \varepsilon_{up}/\varepsilon_0 = 1$ (uncovered on both sides). Fine agreement is observed.

Another validation case is presented in Fig. 9, again for the $m = -1$ Floquet harmonic, but this time with reference to [33] for $\theta_{inc} = 30°$, $\phi_{inc} = 0$, $d_x = 4\,\text{mm}$, $\varepsilon_{grv}/\varepsilon_0 = 4$, $h = 1.6\,\text{mm}$, $g = 2.4\,\text{mm}$, $a_{up} = a_{\ell o} = g$, and $\varepsilon_{\ell o}/\varepsilon_0 = \varepsilon_{up}/\varepsilon_0 = 1$. Once more, the results obtained by the present modal technique cohere well with those of standing literature.

5. CONVERGENCE OF THE NUMBER OF MODES

There are two types of modes in the modal approach: those of the parallel-plate waveguide cavity sections, and of Floquet harmonics associated with the periodicity of the structure. How the number of each kind, henceforth denoted as N_{cav} and N_{Floq} respectively, affects the computed transmission and reflection spectra will be studied. The N_{cav} is the truncated largest modal integer for each of both the TE and TM modal cavity modes, whereas the Floquet harmonic integers span from $-N_{Floq}$ to N_{Floq} through 0, in steps of unity.

For the same topology as Fig. 5, each left and right side subplot in Fig. 10 presents, for a certain N_{cav} as labeled within, the transmission and reflection spectra, respectively, for six numbers of Floquet modes, namely N_{Floq} ranging from 1 through 6, as annotated. The upper and lower pair of panels in the figure are for $N_{cav} = 1$ and 2, respectively. Also included within every graph is the so-called correctly converged reference trace entailing $N_{cav} = 10$ and $N_{Floq} = 12$ which concurs with the simulation results from the commercial CST software in Fig. 5. Observing the upper pair of plots pertaining to $N_{cav} =$

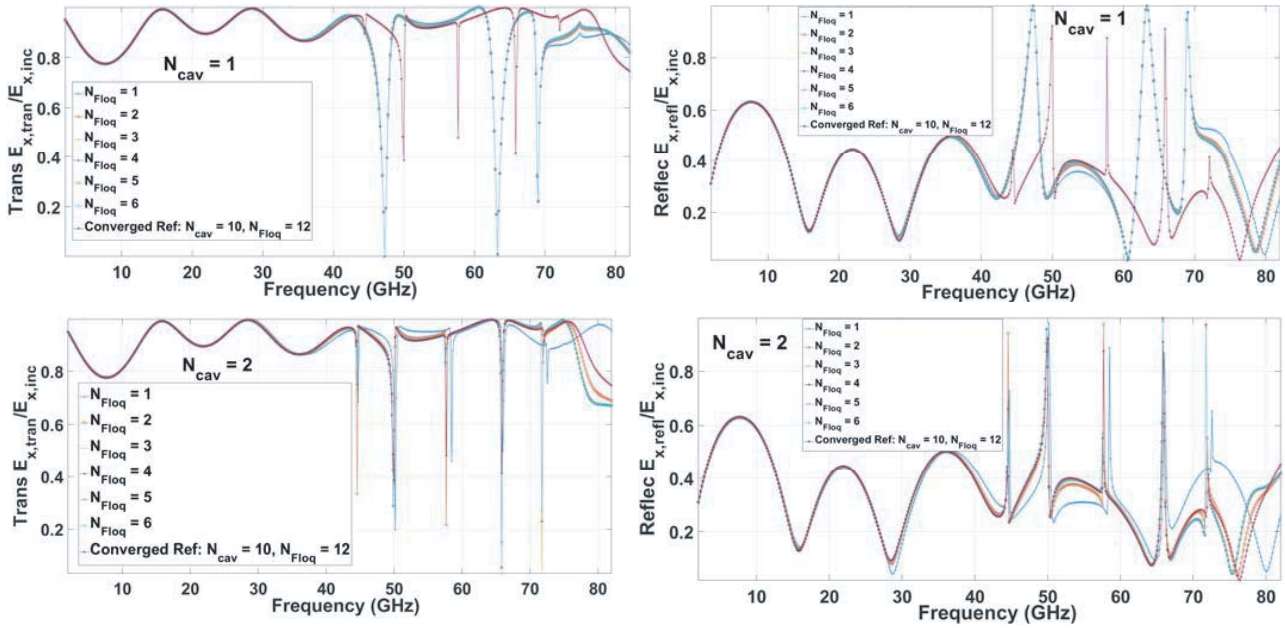

Figure 10. Transmission and reflection spectra of the case of Fig. 5 for various numbers of cavity modes and Floquet harmonics (N_{cav} & N_{Floq}) considered in the computation: each panel pertains to certain N_{cav} and displays traces for N_{Floq} = 1, 2, 3, 4, 5 & 6 as annotated. Upper pair of panel: N_{cav} = 1, lower pair: N_{cav} = 2.

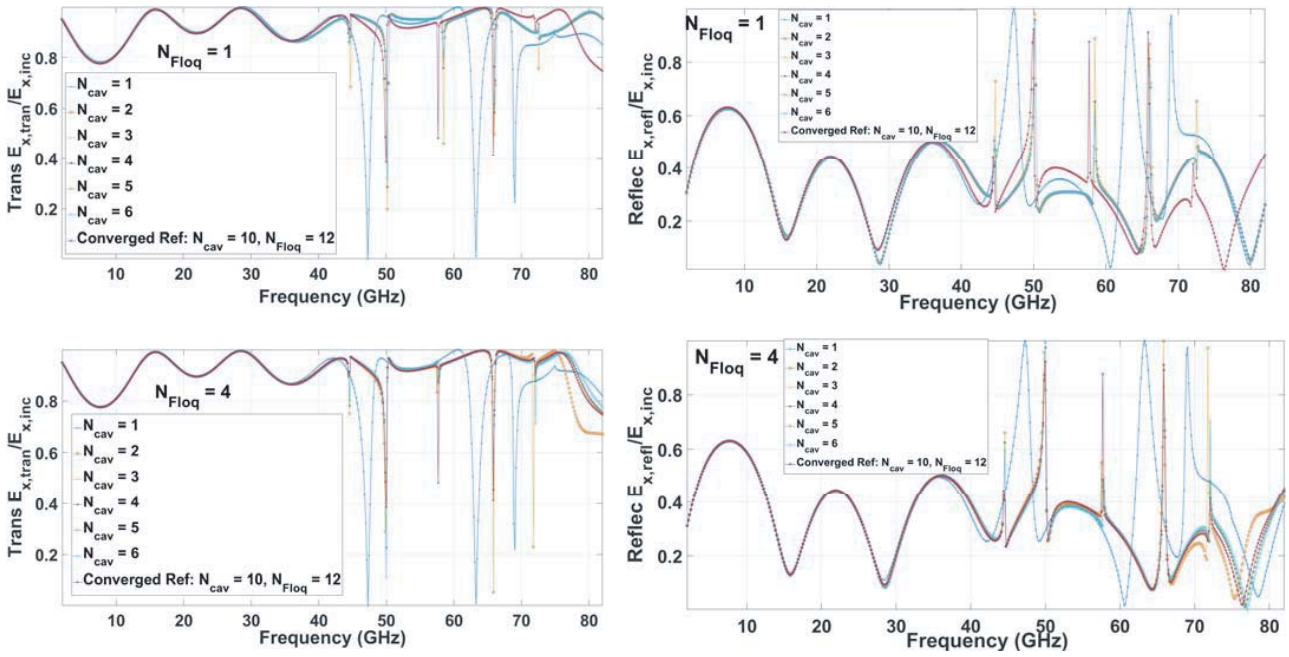

Figure 11. Transmission and reflection spectra of the case of Fig. 5 for various numbers of Floquet harmonics and cavity modes (N_{Floq} & N_{cav}) considered in the computation: each panel pertains to certain N_{Floq} and displays traces for N_{cav} = 1, 2, 3, 4, 5 & 6 as annotated. Upper pair of panel: N_{Floq} = 1, lower pair: N_{Floq} = 4.

1, although the traces converge to one another abruptly right upon the increment from $N_{Floq} = 1$ to 2, the bundled curves do not yet agree well with the correctly converged reference regardless of how high N_{Floq} gets. It is only with $N_{cav} = 2$ in the lower pair of plots that results which cohere adequately well with the correct reference are achieved by $N_{Floq} > 4$. Cases for larger values of N_{cav} have been computed but are not presented. But they all also portray convergence behaviors consistent with the above observations.

Swapping the two types of modes, each panel in Fig. 11 now presents, for a certain N_{Floq}, the transmission and reflection spectra for six values of N_{cav}, namely $N_{cav} = 1$, 2, 3, 4, 5 & 6 as annotated, again for the structural case of Fig. 5. As before, the correctly converged reference trace is included in each subplot. Observing the upper pair of plots associated with $N_{Floq} = 1$, only the curve of $N_{cav} = 1$ in each of both graphs is distinctly dislodged from the rest that are closely-overlapping, but yet, none of these latter has approached closely enough to the correctly converged reference. It takes an N_{Floq} of 4 in order for proper convergence to be attained by as few as $N_{cav} = 2$, as the lower pair of panels demonstrate.

6. CONCLUSIONS

An accurate full-wave modal approach to analyze and numerically treat corrugations with strip-loaded ridges which are sheathed on both sides by multiple layers of dielectric slabs has been presented. In the moment method framework, the fields inside the grooves are obtained by parallel-plate dyadic waveguide cavity Green's functions whereas those within the exterior stratified media are derived from spectral domain Green's functions for planar multilayer structures, which rest upon classical concepts of Floquet theory and the surface equivalence theorem. By the PEC equivalence theorem, mode-matching between the two regions may then ensue. Among the graphs that have been computed by the code developed according to this numerical technique include those that portray how the transmission and reflection coefficients of any Floquet modal harmonic (or diffraction order) vary with any prescribed parameter, as well as surface-wave modal dispersion diagrams. These results have been rigorously validated with an independent commercial solver as well as results from literature.

Higher ordered diffraction modes that have been focused here other than the fundamental Floquet harmonic are those of $m = -1$ and $+1$, which are typically the two most relevant ones in the context of numerous applications ranging from mode converters and beam deflectors to grating couplers, pulse compression gratings, and diffraction gratings in spectroscopy. The capabilities of these applications such as the enhancement of transmission of the higher order Floquet harmonics, as well as the bandwidth and scan-width over which this is achieved can be improved by tailoring the new parameters of the special configuration.

ACKNOWLEDGMENT

This work was partially supported by the "Center for mmWave Smart Radar Systems and Technologies" under the Featured Areas Research Center Program within the framework of the Higher Education Sprout Project by the Ministry of Education (MOE) in Taiwan, and partially supported by the Ministry of Science and Technology (MOST) of Taiwan under Grant numbers MOST 109-2634-F-009-030 and 107-2221-E-009-051-MY2.

REFERENCES

1. Flanders, D. C., H. Kogelnik, R. V. Schmidt, and C. V. Shank, "Grating filter for thin film optical waveguides," *Appl. Phys. Lett.*, Vol. 24, 194–196, 1974.
2. Schmidt, R. V., D. C. Flanders, C. V. Shank, and R. D. Standley, "Narrow band grating filters for thin film optical waveguides," *Appl. Phys. Lett.*, Vol. 25, 651–652, 1974.
3. Tamir, T. and H. L. Bertoni, "Lateral displacement of optical beams at multilayered and periodic structures," *J. Opt. Soc. Amer.*, Vol. 61, 1397–1413, 1971.

4. Harris, J. H., R. K. Winn, and D. G. Dalgoutte, "Theory and design of periodic couplers," *Appl. Opt.*, Vol. 11, 2234–2241, 1972.
5. Peng, S. T., T. Tamir, and H. L. Bertoni, "Leaky wave analysis of optical periodic couplers," *Electron. Lett.*, Vol. 9, 150–152, 1973.
6. Kuhn, L., P. F. Heidrich, and E. G. Lean, "Optical guided wave mode conversion by an acoustic surface wave," *Appl. Phys. Lett.*, Vol. 19, 428–430, 1971.
7. Sasaki, H., I. Kushibiki, and N. Chubachi, "Efficient acousto-optic TE-TM mode conversion in ZnO films," *Appl. Phys. Lett.*, Vol. 25, 476–477, 1974.
8. Ohmachi, Y., "Acousto-optic TE-TM mode conversion in a thin film of amorphous tellurium dioxide," *Electron. Lett.*, Vol. 9, 539–541, 1973.
9. Tseng, S. C. C., A. R. Reisinger, E. A. Geiss, and C. G. Powell, "Mode conversion in magneto-optic waveguides subjected to a periodic permalloy structure," *Appl. Phys. Lett.*, Vol. 24, 265–267, 1974.
10. Gia Russo, D. P. and J. H. Harris, "Electro-optic modulation in a thin film waveguide," *Appl. Opt.*, Vol. 10, 2786–2788, 1971.
11. Polky, J. N. and J. H. Harris, "Electro-optic thin film modulator," *Appl. Phys. Lett.*, Vol. 21, 307–309, 1972.
12. Tien, P. K., R. J. Martin, R. Wolfe, R. C. LeCraw, and S. L. Blank, "Switching and modulation of light in magneto-optic waveguides of garnet films," *Appl. Phys. Lett.*, Vol. 21, 294–396, 1912.
13. Kuhn, L., M. L. Dakss, P. F. Heidrich, and B. A. Scott, "Deflection of an optical guided wave by a surface acoustic wave," *Appl. Phya Lett.*, Vol. 17, 265–267, 1970.
14. Giallorenzi, T. G. and A. F. Milton, "Light deflection in multimode waveguides using the acousto-optic interaction," *J. Appl. Phys.*, Vol. 45, 1762–1774, 1974.
15. Wille, D. A. and M. C. Hamilton, "Acoustoaptic deflection in Ta2O5 waveguides," *Appl. Phys. Lett.*, Vol. 24, 159–160, 1974.
16. Luukkala, M. and P. Merilainen, "Image scanning by acousto-electro-optic interaction," *Elect. Lett.*, Vol. 10, 80–81, 1974.
17. Yamamoto, Y., T. Kamiya, and H. Yanai, "Improved coupled mode analysis of corrugated waveguides and lasers," *IEEE Journal of Quantum Electronics*, Vol. 14, No. 4, 245–258, Apr. 1978, doi: 10.1109/JQE.1978.1069769.
18. Nakata, Y. and M. Koshiba, "Boundary-element analysis of plane-wave diffraction from groove-type dielectric and metallic gratings," *J. Opt. Soc. Am. A*, Vol. 7, 1494–1502, 1990.
19. Matsumoto, M., "Analysis of radiation properties of channel-waveguide gratings," *J. Opt. Soc. Am. B*, Vol. 8, 434–442, 1991.
20. Butler, J. K., W. E. Ferguson, G. A. Evans, P. J. Stabile, and A. Rosen, "A boundary element technique applied to the analysis of waveguides with periodic surface corrugations," *IEEE Journal of Quantum Electronics*, Vol. 28, No. 7, 1701–1709, Jul. 1992, doi: 10.1109/3.142557.
21. Park, T. J., H. J. Eom, and K. Yoshitomi, "Analysis of TM scattering from finite rectangular grooves in a conducting plane," *J. Opt. Soc. Am. A*, Vol. 10, 905–911, 1993.
22. Nishimoto, M. and H. Ikuno, "Analysis of electromagnetic wave diffraction by a semi-infinite strip grating and evaluation of end-effects," *Progress In Electromagnetics Research*, Vol. 23, 39–58, 1999.
23. Armeanu, A. M., M. K. Edee, G. Granet, and P. Schiavone, "Modal method based on spline expansion for the electromagnetic analysis of the lamellar grating," *Progress In Electromagnetics Research*, Vol. 106, 243–261, 2010.
24. Granet, G., L. B. Andriamanampisoa, K. Raniriharinosy, A. M. Armeanu, and K. Edee, "Modal analysis of lamellar gratings using the moment method with subsectional basis and adaptive spatial resolution," *J. Opt. Soc. Am. A*, Vol. 27, 1303–1310, 2010.
25. Frances Monllor, J., C. Neipp, A. Marquez Ruiz, A. Belendez, and I. Pascual, "Analysis of reflection gratings by means of a matrix method approach," *Progress In Electromagnetics Research*, Vol. 118, 167–183, 2011.
26. Ng Mou Kehn, M., "Moment method analysis of plane wave scattering from planar corrugated surfaces using parallel-plate cavity Green's functions and derivation of analytic reflection-phase

formulas for both polarizations and oblique azimuth planes," *Radio Sci.*, Vol. 47, RS3008, 1–17, Jun. 2012.

27. Ng Mou Kehn, M. and W. Y. Lai, "Modal analysis of gratings with conducting strip-loaded bars and sandwiched between multiple dielectric layers," *IEEE Trans. Antennas Propag.*, Vol. 68, No. 6, 5027–5032, Jun. 2020, doi: 10.1109/TAP.2019.2955214.
28. Balanis, C. A., *Advanced Engineering Electromagnetics*, Wiley & Sons, New York, 1989.
29. Harrington, R. F., *Field Computation by Moment Methods*, IEEE Press, New York, 1993.
30. Ng Mou Kehn, M., "Modal analysis of substrate integrated waveguides with rectangular via-holes using cavity and multilayer Green's functions," *IEEE Trans. Microw. Theory Tech.*, Vol. 62, No. 10, 2214–2231, Oct. 2014.
31. Ishimaru, A., *Electromagnetic Wave Propagation, Radiation, and Scattering*, Chap. 14, Prentice Hall, New Jersey, 1991.
32. Rubin, B. J. and H. L. Bertoni, "Scattering from a periodic array of conducting bars of finite surface resistance," *Radio Sci.*, Vol. 20, No. 4, 827–832, Jul.–Aug., 1985.
33. Gedney, S. D. and R. Mittra, "Analysis of the electromagnetic scattering by thick gratings using a combined FEM/MM solution," *IEEE Trans. Antennas Propag.*, Vol. 39, No. 11, 1605–1614, Nov. 1991.